

How well do cosmological simulations reproduce individual-halo properties?

Michele Trenti¹, Britton D. Smith, Eric J. Hallman, Samuel W. Skillman, J. Michael Shull

University of Colorado, CASA, Dept. of Astrophysical & Planetary Sciences, 389-UCB, Boulder, CO 80309, USA

ABSTRACT

Cosmological simulations of galaxy formation often rely on prescriptions for star formation and feedback that depend on halo properties such as halo mass, central over-density, and virial temperature. In this paper we address the convergence of individual halo properties, based on their number of particles N , focusing in particular on the mass of halos near the resolution limit of a simulation. While it has been established that the halo mass function is sampled on average down to $N \sim 20 - 30$ particles, we show that *individual* halo properties exhibit significant scatter, and some systematic biases, as one approaches the resolution limit. We carry out a series of cosmological simulations using the Gadget2 and Enzo codes with $N_p = 64^3$ to $N_p = 1024^3$ total particles, keeping the same large-scale structure in the simulation box. We consider boxes of small ($l_{box} = 8 \text{ Mpc h}^{-1}$), medium ($l_{box} = 64 \text{ Mpc h}^{-1}$) and large ($l_{box} = 512 \text{ Mpc h}^{-1}$) size to probe different halo masses and formation redshifts. We cross-identify dark matter halos in boxes at different resolutions and measure the scatter in their properties. The uncertainty in the mass of single halos depends on the number of particles (scaling approximately as $N^{-1/3}$), but the rarer the density peak, the more robust its identification. The virial radius of halos is very stable and can be measured without bias for halos with $N \gtrsim 30$. In contrast, the average density within a sphere containing 25% of the total halo mass is severely underestimated (by more than a factor 2) and the halo spin is moderately overestimated for $N \lesssim 100$. If sub-grid physics is implemented upon a cosmological simulation, we recommend that rare halos ($\sim 3\sigma$ peaks) be resolved with $N \gtrsim 100$ particles and common halos ($\sim 1\sigma$ peaks) with $N \gtrsim 400$ particles to avoid excessive numerical noise and possible systematic biases in the results.

Subject headings: methods: N-body simulations — galaxies: formation

¹trenti@colorado.edu

1. Introduction

Cosmological simulations are a fundamental tool for investigating the formation and evolution of dark matter halos and of the resulting galaxies (Bertschinger 1998). With advancements in both memory and computing power capabilities, simulations can now be performed with up to several billion particles. Efforts have been focused both on investigating the formation of single halos with ultra-high resolution (e.g., Diemand et al. 2007; Springel et al. 2008a; Stadel et al. 2009) and on simulating structure formation in large boxes, on the order of Gpc^3 , that represent the large-scale structure in the Universe. (e.g., Springel et al. 2005; Yepes et al. 2008). However, the dynamic range of scales to be resolved is so large, despite the continuous hardware improvements, that numerical simulations need to be pushed to their limits for many interesting problems. For example, to follow the formation of the first stars in the Universe, a sub-solar mass resolution is needed (O’Shea & Norman 2007; Turk et al. 2009). This limits the size of the simulation box to below $\sim 1 \text{ Mpc}^3$, and thus large-scale structure effects are missed. At other range of the spectrum, simulations of the formation of bright (and thus rare) high-redshift quasars observed in all-sky surveys such as the Sloan Digital Sky Survey (Fan et al. 2006) require computational volumes $\geq 10^9 \text{ Mpc}^3$ and resolution sufficient to identify the black hole seeds from metal-free stars, for a total dynamic range $\geq 10^{12}$ (Trenti & Stiavelli 2007; Trenti et al. 2008). Under such conditions, information from barely resolved halos needs to be used. In addition, sub-grid physics recipes are often employed, either in the form of semi-analytical (post-processing) modeling (Kauffmann & Charlot 1998; Somerville & Primack 1999; De Lucia & Blaizot 2007) or as star formation and feedback recipes implemented during the run (Springel & Hernquist 2003; Oppenheimer & Davé 2008).

Therefore, convergence and validation of the numerical methods used are of fundamental importance to establish the reliability of the conclusions drawn from numerical experiments. Past investigations have addressed two fundamental issues regarding dark matter (DM) halos: the convergence of the inner slope of the density profile and the accuracy of the halo mass function. The inner-slope problem, arising from the absence of observational evidence of the density cusps predicted in simulations (Navarro et al. 1997), has been the focus of several studies using extremely high resolution (Ghigna et al. 2000; Power et al. 2003; Fukushige et al. 2004), but the issue appears to be settled, with the inner regions expected to follow a Einasto density profile (Navarro et al. 2010; Stadel et al. 2009). Regarding the DM halo mass function, it is now well established that a cosmological simulation reproduces with fidelity the mass function down to halos with $N \gtrsim 20 - 30$ particles (Reed et al. 2003; see also Heitmann et al. 2006; Warren et al. 2006; Lukić et al. 2007), although there can be box-size effects (Bagla & Ray 2005; Reed et al. 2007, 2009). These results are also in excellent agreement with analytical predictions (Sheth & Tormen 1999; Jenkins et al. 2001).

As we will demonstrate, the mass function is only an average property of the halo mass distribution. A much deeper question pertains to the reliability of properties of single halos, derived from a simulation with given resolution, with a goal similar to the study of subhalos properties in the Aquarius run (Springel et al. 2008a; Springel et al. 2008b). Individual halo properties affect the variance of the results derived from the simulations (Warren et al. 2006). For example, if semi-analytical formulae and/or star formation recipes are implemented in a run, the uncertainty on individual halos propagates to the derivation of quantities such as the star formation rate, the fundamental plane thickness (Djorgovski & Davis 1987) or the tightness in the relation between the central black hole mass and bulge velocity dispersion (Ferrarese & Merritt 2000).

The goal of this paper is to quantify the numerical scatter and identify possible biases in the mass of individual halos as a function of the number of particles in the halo. Past investigations have characterized the behavior of halo finders for idealized systems with small N , for example by generating discrete realizations of a Navarro et al. (1997) profile or by downsampling the resolution of a simulation snapshot (Warren et al. 2006; Lukić et al. 2009). We extend these studies by studying the convergence of halo properties in a fully cosmological context, where the convergence properties of the N -body integration are also investigated. We carry out a suite of simulations, where higher resolution boxes are constrained to have the same phases as low-resolution versions. We cross-identify halos between the different runs and measure convergence of their properties, which turns out to be different with respect to the more idealized numerical experiments of Warren et al. (2006) and Lukić et al. (2009). Our study should help the community of numerical cosmologists to quantify the limit at which they should trust their simulations, depending on the desired accuracy goal.

This paper is organized as follows. In Section. 2 we introduce the setup of our suites of simulations, whose results are presented in Section. 3. We conclude in Section. 4 by discussing our recommendations for the minimum resolution required for implementing extra physics on dark matter halos.

2. Numerical setup

We generate initial conditions using the *Grafic1* package (Bertschinger 2001), with a custom modification that allows us to apply the Hoffman & Ribak (1991) method over the full simulation box and to use the Eisenstein & Hu (1999) power-spectrum fitting formula. With our customization, we are able to start from a low-resolution version of the initial conditions and then refine it to higher resolution while keeping the same large-scale structure. We use a WMAP-5 cosmology (Komatsu et al. 2009) with $\Omega_\Lambda = 0.72$, $\Omega_m = 0.28$, $\Omega_b =$

0.0462, $\sigma_8 = 0.817$, $n_s = 0.96$ and $h = 0.7$. We consider three different box sizes: a small box of edge $l_{box} = 8 \text{ Mpc } h^{-1}$, a medium box (edge $l_{box} = 64 \text{ Mpc } h^{-1}$) and a large box ($l_{box} = 512 \text{ Mpc } h^{-1}$). The simulations have a range of total particles from $N_p = 64^3$ to $N_p = 1024^3$ (the number of particles in a single halo is instead indicated as N). The small-box simulations start at redshift $z = 199$, while the medium and large-box simulations begin at $z = 100$. The boxes have periodic boundary conditions. Details on the specific simulations, including their mass resolution, are shown in Table 1.

As our code of choice we use the particle-mesh tree code Gadget2 in its “lean” version (Springel 2005; Springel et al. 2005) to carry out dark-matter only simulations. The softening parameter is set to $\epsilon = l_{box}/(42.5N_p)$, allowing us to achieve a good spatial resolution of virialized halos with a small number of particles. For comparison, we also carry out a subset of the runs (the medium-box series) using the hydrodynamic code Enzo (Bryan et al. 1995). Enzo² uses the block-structured adaptive mesh refinement (AMR) scheme of Berger & Colella (1989) to achieve high spatial and temporal resolution, and it combines an N-body adaptive particle-mesh solver for dark matter dynamics with a Piecewise Parabolic Method (PPM) hydro solver that has been optimized for cosmological applications (Colella & Woodward 1984; Bryan et al. 1995). Because our primary goal is to test the DM halo dynamics of Enzo, we do not include gas in the Enzo simulations. The number of top-grid cells in our Enzo runs is equal to the total number of particles.

The main difference between the Gadget2 and Enzo under these conditions is their spatial resolution. The force resolution in Enzo is twice the grid size, that is $2l_{box}/N_p^{1/3}$. In Gadget2, the force becomes unsoftened at a distance of about 3ϵ , or at $\sim l_{box}/(14N_p^{1/3})$ in our simulations. The Gadget2 runs thus have about 30 times better spatial resolution than their Enzo counterparts, if a uniform grid and no AMR is used in Enzo. To investigate the effect of force resolution on the properties of halos, we have carried out a subset of the Enzo runs ($N_p = 64^3$ to $N_p = 256^3$) allowing up to six levels of AMR. This improves the force resolution by a factor up to 2^6 , thereby reaching a maximum force accuracy comparable to that attained by Gadget2. Enzo still has a lower force resolution in regions with overdensities below the critical threshold for AMR (see O’Shea et al. 2005). While many applications of Enzo rely on aggressive use of AMR, for example in the context of the formation of Population III stars (O’Shea & Norman 2007; Turk et al. 2009), a growing number of investigations consider runs with uniform resolution (Regan et al. 2007; Paschos et al. 2009; Tytler et al. 2009; Norman et al. 2009). Especially for studies of the Ly α forest, it has been shown by Regan et al. (2007) that disabling AMR provides an order-of-magnitude speedup, while only

²<http://lca.ucsd.edu/projects/enzo>

introducing $\sim 5\%$ errors in the Ly α flux power spectrum.

We save snapshots of the simulations at regular redshift intervals ($z = 6, 4, 1, 0$) and we identify DM halos with a friends-of-friends (FoF) algorithm (Davis et al. 1985) with linking length 0.2. We also analyze a subset of runs with the Amiga halo finder (Knollmann & Knebe 2009) that includes a boundness check for the halo particles. In addition, the Amiga halo finder provides detailed information on each halo, including their density profile and spin parameter.

We consider halos with at least 32 particles. To cross-identify the same halo in two simulations at different resolution, we match individual particle identification numbers (IDs) that are representative of the initial particle positions. Our method is similar to that discussed in Springel et al. (2008a). The ID of every particle in the lower resolution realization (with $N = N_{low}$) is used to calculate its corresponding $n_c = N_{high}/N_{low}$ “child”³ particle IDs in the high-resolution simulation (with $N = N_{high}$). From the list of particle IDs in each halo we can thus ascertain whether that halo has one or more counterparts in the higher-resolution run. Similarly, given a halo in the high-resolution simulation, we can determine the presence of any low-resolution counterparts. Note that the relation between halos in snapshots at two different resolutions is not necessarily one-to-one or one-to-zero. In fact, multiple halos can be the counterparts of a single larger halo, especially in the process of merging. For any given low-resolution halo, we identify its high-resolution counterpart by considering the high-resolution halo that has the largest number of individual “children” particle matches. In passing we note that if matching of halos is based instead on their positions, there is no guarantee of either positive or unique identification. This affects especially common low-mass objects in the proximity of larger halos, because a change in resolution can lead to different tidal forces and changes in the rate of mergers.

3. Results

In Figure 1 we show the scatter of individual halo masses in our medium-box simulation at $z = 0$ when the resolution progressively increases from $N_p = 64^3$ to $N_p = 512^3$. We plot the ratio of low-to-high resolution mass of halos M_{low}/M_{512} as a function of the halo mass in the highest-resolution run M_{512} . As the resolution is increased, it is clear that the halo mass is measured with progressively higher accuracy. In Figure 2 we show the scatter as a function

³If the N_p is increased by 2^3 , then each low-resolution particle has 2^3 counterparts, or “children” at high-resolution. The average position and velocity of the “children” corresponds approximately, but not exactly, to the position and velocity of their low-resolution “parent” (Bertschinger 2001).

of the number of particles in the low resolution run (N_{low}). The median mass of halos is correct down to about 100 particles, while it tends to be underestimated for the smallest halos. However, the halo mass function remains consistent as shown in Figure 3 (see also Reed et al. 2007). We quantify the dimensionless scatter, $\xi(N_{low})$, around the median for halos with N_{low} particles by considering one half of the symmetric 1σ interval that encloses from 16% to 84% of the M_{low}/M_{high} points for halos with $N_{low} - \Delta N \leq N \leq N_{low} + \Delta N$. We chose $\Delta N \gtrsim 10$ adaptively to ensure that the distribution is well sampled. The scatter around the median grows steadily as the number of particle decreases. For halos with less than 10^3 particles, their mass has $\gtrsim 20\%$ uncertainty at 68% confidence level. The convergence of the mean halo mass down to a small number of particles is consistent with previous resolution studies (Reed et al. 2003) that demonstrated that the halo mass function of a simulation is correctly sampled down to such low particle number.

Although the mean halo properties we find are consistent with those reported in earlier investigations, the individual scatter of halo masses measured from cosmological simulations differs from the estimates based on idealized experiments carried out by Warren et al. (2006) and Lukić et al. (2009). First, both Warren et al. (2006) and Lukić et al. (2009) report that FoF halo finders tend to overestimate the mass of discrete realizations of a halo at low N . In actual simulations, the opposite behavior is observed. The mass of small N halos is in fact underestimated at low resolution. By comparing the $N_p = 256^3$ realization of the medium box against the $N_p = 512^3$ realization, we find that the average of M_{low}/M_{high} for halos with $32 \leq N \leq 64$ is 0.84 and the median is 0.77. From Table 1 and Equation 3 of Warren et al. (2006) we would have instead expected $\langle M_{low}/M_{high} \rangle \gtrsim 1.1$. We obtain a different result because the mass of the halo in a simulation depends not only on the convergence properties of the halo-finder algorithm, explored by Warren et al. (2006) and Lukić et al. (2009), but also on those of the code that resolves the non-linear gravitational dynamics leading to the formation of the halos. A lower number of particles, and thus a reduced force and spatial resolution, suppresses high frequency modes of the effective power spectrum of the simulation, producing an underestimate of the mass of halos near the resolution limit of the run (see also O’Shea et al. (2005) for a similar finding in the context of the comparison between Enzo and Gadget2). A second difference between our findings and those published earlier is in the amplitude of the scatter. Both Warren et al. (2006) and Lukić et al. (2009) observe in their halo experiments a scatter in the measure of halo masses that is a factor 2 lower than what is realized in a cosmological simulation. For example, Warren et al. (2006) measure an 18% relative $1-\sigma$ error for their synthetic $N = 50$ halos. In our simulations, the $1-\sigma$ relative error is $\gtrsim 55\%$ for halos with $N \sim 50$ as shown in the bottom left panel of Figure 2. Again, this is not surprising, because our results are affected primarily by the different resolution in the cosmological simulations, rather than by the convergence properties of the halo finder.

Interestingly, the considerable scatter in the individual halo mass is left essentially unchanged if the DM halo catalogs are pruned of unbound particles when $N \gtrsim 100$. This is shown in the right panels of Figure 2, which are the equivalent of the left panels but obtained using halo catalogs from the Amiga halo finder that includes a boundness check for membership of particles to a halo (Knollmann & Knebe 2009). Removing unbound particles helps only at the lowest end of the resolution for halos with $N \lesssim 100$; for example $\xi_{Amiga}(N = 40) \sim 0.4$ while $\xi_{FoF}(N = 40) \sim 0.55$. As expected, the overall number of halos identified in a snapshot above a given halo mass is slightly lower ($\sim 5\%$) when unbound particles are removed. For example, in the medium box with $N_p = 512^3$ particles, there are 98,011 halos with $N \geq 32$ particles identified by the friends-of-friends halo finder and 93,364 by the Amiga halo finder at $z = 0$.

The scatter in halo masses remains largely unchanged when we consider different box sizes and redshifts, as shown in Figure 4. There is a moderate tendency for rare halos to be better resolved at a given number of particles compared to their more common counterparts, especially when $N \lesssim 10^2$ (see Figure 5). This is highlighted by quantifying the rarity of halos using the extended Press-Schechter variable $\nu = \delta_c^2/\sigma^2(M)$. For example, the very common (low ν) halos in Figure 5 have considerable more scatter at $N \sim 100$ than rarer halos (high ν) with a similar number of particles. In addition, common halos with $\sim 10^2$ particles may be in reality part of a larger halo when the numerical resolution is increased (see the points at $M_{\text{low}}/M_{\text{high}} \sim 0$ in the bottom left panel of Figure 2). This effect does not happen for rarer halos (see the upper left panel of Figure 2). This is not surprising, because if a halo originates from a rare peak, then it is more likely to be the dominant gravitational source in its surroundings and the dynamics of its own particles is primarily governed by self-gravity. In contrast, more common halos are likely to be surrounded by at least comparably massive neighbors, and they might be more affected by tidal-field errors.

The scatter of individual halo masses is reduced as the number of particles in a halo increases, but it remains considerable, even when a halo has $N \gtrsim 10^3$ particles (see Figure 6). The scaling of convergence with the number of particles can be understood with a simple analytical model. For the purpose of computing the total mass of a halo, the particles more likely to be affected by errors in their dynamics are those initially located at the periphery of the halo over-density. In the linear regime at $z \gg 1$, when the density field is quasi-homogeneous, a spherical region that contains N particles has N_{boundary} edge particles, where:

$$N_{\text{boundary}} \approx 4\pi \left(\frac{3N}{4\pi} \right)^{2/3}. \quad (1)$$

Assuming that a fraction of the edge particles is affected by numerical resolution, then the dispersion of the mass of an individual halo scales as $\xi(N) \propto N_{\text{boundary}}/N \sim N^{-1/3}$. If

we assume that, on average, about half of the edge particles are susceptible to change of membership when the resolution is increased, then we expect a $\sim 20\%$ uncertainty in the mass of a halo with $1000 \leq N \leq 2000$ particles, in reasonable agreement with the scatter we measure ($\sim 15\%$ in Figure 5). This means that to reduce the typical uncertainty on a halo mass below 10%, $N \sim 5000$ particles are required. Because this scaling depends only on the surface-to-volume ratio, the $N^{-1/3}$ trend is predicted even if the spherical assumption for the collapse is relaxed and more realistic models for the formation of halos are considered, such as the ellipsoidal collapse model (Sheth et al. 2001). Figure 6 shows that the empirical measurements for $\xi(N)$ do indeed show that a good fit of the overall distribution is given by:

$$\xi(N) \sim 0.15 \left(\frac{N}{1000} \right)^{-1/3}. \quad (2)$$

From Figures 1 and 2 it can be seen that some halos with a large number of particles ($N \gtrsim 10^4$) can occasionally have a large variation in their mass when the same box is resimulated at higher resolution. These are halos in the process of merging, as shown in Figure 7 for a halo with 8192 particles in the $l_{box} = 64\text{Mpc } h^{-1}$ box ($N_p = 256^3$) at $z = 0$. While the FoF halo finder flags the halo as a single entity at low resolution (there is a bridge of particles connecting the two main components), at high resolution the merging is slightly delayed, so that the two sub-components are still separate halos. Of course, the opposite condition may also be realized, with two individual halos identified at low resolution and a single halo at high resolution. Such ambiguity in defining a halo cannot be avoided unless an additional diagnostic is used in addition to halo-finding algorithms (such as halo profilers or indicators for an irregular morphology). Nevertheless, the fraction of halos in the process of undergoing a merger in any single snapshot is small, and the measure of $\xi(N)$ is not affected by outliers in the distribution of M_{low}/M_{high} .

The dimensionless scatter ξ we measure appears larger by about a factor two compared to the scatter quantified for subhalos in the *Aquarius* simulation (Figure 16 in Springel et al. 2008a; see also the supplementary information in Springel et al. 2008b). The better convergence of subhalo properties found by Springel et al. (2008a) is not surprising. In fact, subhalos are the remnants of initially more massive halos that have been stripped of their less bound particles, both during the merging with the main halo and by tidal forces, once the subhalo is orbiting inside the parent halo. Loosely bound particles are more likely to be added or removed from a halo as a result of a change in resolution. In addition, once a subhalo is part of a larger halo, its orbit becomes defined by the parent halo potential, and further merging with other subhalos is highly unlikely. Scatter in the individual properties of subhalos is thus not affected by the ambiguity in defining a halo undergoing a major merger, contrary to what might happen for the halos studied here (Figure 7).

The convergence of individual halo properties appears worse in Enzo runs when $N \lesssim 400$. Figure 3 shows that the halo mass function of such runs deviates from both the analytical Sheth & Tormen (1999) prediction and the higher-resolution realization when $N \lesssim 400$. Increasing the force resolution by switching on AMR helps with respect to Enzo Unigrid runs, but there is still a significant number of halos missing at $N \lesssim 400$. This trend identified in the halo mass function is also clearly visible at the level of individual halo masses (see Figure 8). The median of the distribution of M_{low}/M_{high} approaches 1 only at $N \sim 1000$, in sharp contrast to the better convergence properties found in the Gadget2 runs. This result is not surprising and has been already previously noted (O’Shea et al. 2005; Hallman et al. 2007). The gravity solver in the Enzo code does in fact suppress small-scale power at very high redshift, before AMR refinement is triggered (O’Shea et al. 2005). The convergence of the halo mass can be improved by increasing the dimension of the top-level grid, as shown by O’Shea et al. (2005). However, this might not always be possible for the largest runs, when the limiting factor of computational resources is often the availability of memory rather than processor speed.

Figure 9 show the convergence of other individual halo properties, obtained by profiling the halos with the Amiga halo finder. The core density (ρ_{25}), defined as the average density within the radius containing 25% of the total halo mass, is reported in Figure 9 for one snapshot at $z = 0$ from the medium box. As expected, the errors on ρ_{25} are larger than those on the total halo mass, and there is clearly a systematic bias: low-resolution halos with small N have a significantly lower ρ_{25} compared to their realization at higher resolution. The median of $\rho_{25\ low}/\rho_{25\ high}$ is as low as ~ 0.3 for $N \sim 32$. This bias has a major impact if the rate of star formation is scaled from the core density, for example by using the Schmidt (1959) law. The systematic underestimation of core density in low-resolution runs is likely due to two-body relaxation at the center of poorly resolved halos. The scatter of the virial radius, r_{vir} , is shown in Figure 9. This quantity appears to be well defined, and has no bias and a small scatter down to $N = 32$. The stability of r_{vir} is not surprising as $r_{vir} \propto M^{1/3}$. Hence, an error on the mass does not severely affect the associated radius. Figure 9 shows the spin of individual halos, measured by the dimensionless parameter $\lambda = J|E|^{1/2}/GM^{5/2}$, where J is the angular momentum of the halo, E its total energy (gravitational and kinetic) and G the gravitational constant. At small N , λ_{low} appears systematically higher than λ_{high} and has a large scatter. This is not surprising: small N systems always have some residual angular momentum, even if the particle positions and velocities were to be drawn from the distribution function of a non-rotating system. The bias in λ for small N may be important in semi-analytic modeling of galaxy formation, in case the angular momentum of a halo is used to determine the presence of a disk.

4. Conclusions and Discussion

In this paper we quantify the convergence of individual halo properties, as the resolution of a cosmological simulation is increased while maintaining the same large-scale structure of the coarser run. We confirm past investigations of the convergence of the global mass function down to our resolution limit of $N = 32$ particles in runs carried out with the particle-mesh tree code Gadget2. At the same time, we demonstrate that the scatter in individual halo masses measured from our set of cosmological simulations is qualitatively and quantitatively different from that reported based on the analysis of the Friends-of Friends halo finder on mock halos and on downsampled snapshots of an individual cosmological simulation (Warren et al. 2006; Lukić et al. 2009). Those experiments highlighted the tendency of the FoF halo finder to *overestimate* the mass of poorly resolved halos. We show instead that, in an actual resolution study of cosmological simulations, the mass of low- N halos tends to be *underestimated*. This behavior in the convergence of low N halo properties is determined primarily by the finite accuracy of the gravity integration, rather than by the properties of the FoF algorithm explored in Warren et al. (2006); Lukić et al. (2009). In fact, the results obtained in Figure 2 with the Amiga halo finder (Knollmann & Knebe 2009) are fully consistent with those obtained with the FoF finder, despite the fact that Amiga identifies halos from the topology of isodensity contours.

In addition to the different direction of the systematic bias, the scatter in the individual halo masses is more than a factor two higher than reported previously for idealized halos. The mass of halos resolved with $N \sim 1000$ particles shows a $\sim 15\%$ scatter when the halos are resimulated at higher ($8\times$) resolution. Halos with a smaller number of particles have a larger uncertainty in their masses, typically of the order of $\sim 30\%$ for $N \sim 100$. The 1σ relative uncertainty in the mass of a single halo with N particles scales approximately as $\xi \sim N^{-1/3}$ (see Eq. 2 and Figure 6). As the resolution limit of the simulation is approached, halo masses show less scatter if the small- N halos are rare, and thus the simulation box is mostly composed of particles still near the regime of linear evolution. The mass of rarer halos can instead be measured relatively well, even with a low number of particles (see Fig. 5). The core density and the spin of small- N halos exhibit a systematic bias in addition to significant scatter. The virial radius of a halo appears to be the quantity with the smallest scatter, no bias down to $N = 32$.

We carried out our analysis using a code — Gadget2 — that can efficiently reach a high force resolution (a small fraction of the initial inter-particle distance) at low computational cost. Simulations done with the AMR code Enzo are prone to a systematic bias in individual halo mass when $N \lesssim 1000$. Resorting to Adaptive Mesh Refinement lessens but does not resolve this problem (see Figure 8). Increasing the top-grid dimension helps to improve

convergence of individual halo masses with $N \sim 100$ (see O’Shea et al. 2005).

Our investigation highlights the importance of carrying out careful resolution studies to validate the conclusions of numerical simulations. This is particularly important when sub-grid physics recipes are implemented within a numerical simulation or when analytical models of galaxy formation are constructed from the simulation snapshots. If these recipes prescribe to populate halos with a small number of particles, one might obtain the correct average behavior of the sample (because the halo-mass function converges down to halos with ~ 30 particles). However, the limited numerical resolution is likely to introduce extra scatter in the properties of the end-products of such simulations. This extra scatter may also propagate from low- N progenitors to descendant halos (and galaxies) of larger mass, for instance if the star-formation recipes depend critically on the initial metal enrichment.

Furthermore, systematic biases are possible. One obvious example is the rate of star formation calculated from the central density of a halo. Figure 9 clearly shows that the core density of halos with $N \lesssim 400$ is underestimated by more than 20% (and by more than 75% at $N \sim 32$). Even recipes based on halo mass alone can lead to systematic biases. One example is the ratio of Ly- α to stellar luminosity in a simple model where the stellar luminosity is proportional to the halo mass, while the Ly- α luminosity depends on $M_{HI}^2 \propto M^2$ (Dayal et al. 2009). The non-linear relation of Ly- α luminosity on the halo mass is therefore affected by the scatter in M_{low}/M_{high} . For example, in our medium-box 256vs512 simulations at $z = 0$, $\langle M_{low}/M_{high} \rangle \sim 0.84$ while $\langle (M_{low}/M_{high})^2 \rangle \sim 1.33$ for halos with $32 \leq N \leq 64$. This means that the Ly- α luminosity would be overestimated compared to the stellar luminosity by a factor ~ 1.6 at low resolution.

Another example is given by the convergence study carried out in Trenti et al. (2009) to validate their simulations for the transition from metal-free to metal-enriched star formation during the reionization epoch. They found that a “low” resolution run ($N_p = 512^3$) achieved full convergence with the high-resolution run ($N_p = 1024^3$) only at $z \lesssim 7$, when sub-grid physics was implemented in DM halos with $N \gtrsim 100$ particles (see Fig. 6 in Trenti et al. 2009). Individual scatter in halo masses might also introduce numerical noise when feedback is considered. For example, if supernova feedback from star formation at the center of the halos is near the critical level to evacuate most of the baryons, then the numerical uncertainty in the halo mass might play a critical role for the future development of the star formation history in the descendant halos of poorly resolved progenitors.

Overall we recommend implementing extra physics only in halos with $N \gtrsim 100$ for rare halos ($\nu \gtrsim 3$) and $N \gtrsim 400$ for very common halos ($\nu \lesssim 1$). This will guarantee $\xi(N) \lesssim 0.2$ and adequate convergence of other halo properties. If this recommendation is followed, then both the Enzo code and Gadget2 are in a regime where their convergence

properties are similar. Of course, many interesting problems in cosmology require a greater dynamic range than is currently possible to resolve. Thus, implementing extra physics only on halos resolved with $N \gtrsim 100$ particles is not optimal. In such cases, modelers should take precautions to demonstrate convergence of their halo simulations with $N \lesssim 100 - 400$ and avoid extrapolating beyond the range of validity.

We thank Zarija Lukić, Brian O’Shea and Darren Reed for stimulating comments, Steffen Knollmann for his advice on compiling and running the Amiga halo finder code, and an anonymous referee for useful suggestions. We acknowledge support from the University of Colorado Astrophysical Theory Program through grants from NASA (NNX07AG77G) and NSF (AST07-07474). This research was supported in part by the National Science Foundation through TeraGrid awards TG-AST090040 and TG-AST090101.

REFERENCES

- Bagla, J. S. & Ray, S. 2005, MNRAS, 358, 1076
- Berger, M. J. & Colella, P. 1989, Journal of Computational Physics, 82, 64
- Bertschinger, E. 1998, ARA&A, 36, 599
- . 2001, ApJS, 137, 1
- Bryan, G. L., Norman, M. L., Stone, J. M., Cen, R., & Ostriker, J. P. 1995, Computer Physics Communications, 89, 149
- Colella, P. & Woodward, P. R. 1984, Journal of Computational Physics, 54, 174
- Davis, M., Efstathiou, G., Frenk, C. S., & White, S. D. M. 1985, ApJ, 292, 371
- Dayal, P., Ferrara, A., & Saro, A. 2009, ArXiv 0907.4989
- De Lucia, G. & Blaizot, J. 2007, MNRAS, 375, 2
- Diemand, J., Kuhlen, M., & Madau, P. 2007, ApJ, 657, 262
- Djorgovski, S. & Davis, M. 1987, ApJ, 313, 59
- Eisenstein, D. J. & Hu, W. 1999, ApJ, 511, 5
- Fan, X., Strauss, M. A., & Richards, e. a. 2006, AJ, 131, 1203
- Ferrarese, L. & Merritt, D. 2000, ApJ, 539, L9
- Fukushige, T., Kawai, A., & Makino, J. 2004, ApJ, 606, 625
- Ghigna, S., Moore, B., Governato, F., Lake, G., Quinn, T., & Stadel, J. 2000, ApJ, 544, 616
- Hallman, E. J., O’Shea, B. W., Burns, J. O., Norman, M. L., Harkness, R., & Wagner, R. 2007, ApJ, 671, 27
- Heitmann, K., Lukić, Z., Habib, S., & Ricker, P. M. 2006, ApJ, 642, L85
- Hoffman, Y. & Ribak, E. 1991, ApJ, 380, L5
- Jenkins, A., Frenk, C. S., White, S. D. M., Colberg, J. M., Cole, S., Evrard, A. E., Couchman, H. M. P., & Yoshida, N. 2001, MNRAS, 321, 372
- Kauffmann, G. & Charlot, S. 1998, MNRAS, 294, 705

- Knollmann, S. R. & Knebe, A. 2009, *ApJS*, 182, 608
- Komatsu, E., Dunkley, J., & Nolta, M. R. e. a. 2009, *ApJS*, 180, 330
- Lukić, Z., Heitmann, K., Habib, S., Bashinsky, S., & Ricker, P. M. 2007, *ApJ*, 671, 1160
- Lukić, Z., Reed, D., Habib, S., & Heitmann, K. 2009, *ApJ*, 692, 217
- Norman, M. L., Paschos, P., & Harkness, R. 2009, *Journal of Physics Conference Series*, 180, 012021
- Navarro, J. F., Frenk, C. S., & White, S. D. M. 1997, *ApJ*, 490, 493
- Navarro, J. F., Ludlow, A., Springel, V., Wang, J., Vogelsberger, M., White, S. D. M., Jenkins, A., Frenk, C. S., & Helmi, A. 2010, *MNRAS*, in press
- Oppenheimer, B. D. & Davé, R. 2008, *MNRAS*, 387, 577
- O’Shea, B. W., Nagamine, K., Springel, V., Hernquist, L., & Norman, M. L. 2005, *ApJS*, 160, 1
- O’Shea, B. W. & Norman, M. L. 2007, *ApJ*, 654, 66
- Paschos, P., Jena, T., Tytler, D., Kirkman, D., & Norman, M. L. 2009, *MNRAS*, 399, 1934
- Power, C., Navarro, J. F., Jenkins, A., Frenk, C. S., White, S. D. M., Springel, V., Stadel, J., & Quinn, T. 2003, *MNRAS*, 338, 14
- Reed, D., Gardner, J., Quinn, T., Stadel, J., Fardal, M., Lake, G., & Governato, F. 2003, *MNRAS*, 346, 565
- Reed, D. S., Bower, R., Frenk, C. S., Jenkins, A., & Theuns, T. 2007, *MNRAS*, 374, 2
- . 2009, *MNRAS*, 394, 624
- Regan, J. A., Haehnelt, M. G., & Viel, M. 2007, *MNRAS*, 374, 196
- Schmidt, M. 1959, *ApJ*, 129, 243
- Sheth, R. K., Mo, H. J., & Tormen, G. 2001, *MNRAS*, 323, 1
- Sheth, R. K. & Tormen, G. 1999, *MNRAS*, 308, 119
- Somerville, R. S. & Primack, J. R. 1999, *MNRAS*, 310, 1087
- Springel, V. 2005, *MNRAS*, 364, 1105

- Springel, V. & Hernquist, L. 2003, MNRAS, 339, 289
- Springel, V., Wang, J., Vogelsberger, M., Ludlow, A., Jenkins, A., Helmi, A., Navarro, J. F., Frenk, C. S., & White, S. D. M. 2008, MNRAS, 391, 1685
- Springel et al. 2008, Nature, 456, 73
- Springel, V., White, S. D. M., & Jenkins, A. e. a. 2005, Nature, 435, 629
- Stadel, J., Potter, D., Moore, B., Diemand, J., Madau, P., Zemp, M., Kuhlen, M., & Quilis, V. 2009, MNRAS, 398, L21
- Trenti, M. & Stiavelli, M. 2007, ApJ, 667, 38
- Trenti, M., Santos, M. R., & Stiavelli, M. 2008, ApJ, 687, 1
- Trenti, M., Stiavelli, M., & Shull, J. M. 2009, ApJ, 700, 1672
- Turk, M. J., Abel, T., & O’Shea, B. 2009, Science, 325, 601
- Tytler, D., Paschos, P., Kirkman, D., Norman, M. L., & Jena, T. 2009, MNRAS, 393, 723
- Warren, M. S., Abazajian, K., Holz, D. E., & Teodoro, L. 2006, ApJ, 646, 881
- Yepes, G., Martinez-Vaquero, L., Khalatyan, A., Gottlöber, S., Hoefft, M., & Teyssier, R. 2008, in IAU Symposium, Vol. 244, IAU Symposium, ed. J. Davies & M. Disney, 393–394

Table 1: Simulation Summary

$N_p^{1/3}$	l_{box}	m_{DM}	z_{start}	z_{end}
128	512 Mpc h^{-1}	$4.98 \times 10^{12} M_\odot h^{-1}$	100	0
256	512 Mpc h^{-1}	$6.22 \times 10^{11} M_\odot h^{-1}$	100	0
512	512 Mpc h^{-1}	$7.78 \times 10^{10} M_\odot h^{-1}$	100	0
1024	512 Mpc h^{-1}	$9.73 \times 10^9 M_\odot h^{-1}$	100	0
64	64 Mpc h^{-1}	$7.78 \times 10^{10} M_\odot h^{-1}$	100	0
128	64 Mpc h^{-1}	$9.73 \times 10^9 M_\odot h^{-1}$	100	0
256	64 Mpc h^{-1}	$1.21 \times 10^9 M_\odot h^{-1}$	100	0
512	64 Mpc h^{-1}	$1.52 \times 10^8 M_\odot h^{-1}$	100	0
128	8 Mpc h^{-1}	$1.90 \times 10^7 M_\odot h^{-1}$	199	6
256	8 Mpc h^{-1}	$2.37 \times 10^6 M_\odot h^{-1}$	199	6
512	8 Mpc h^{-1}	$2.97 \times 10^5 M_\odot h^{-1}$	199	6

Note. — Summary of the properties of our cosmological simulations done with Gadget2. The first column reports the number of dark matter particles N_p , the second the box-size l_{box} . The single-particle dark-matter mass (m_{DM}) is in the third column, the initial redshift z_{start} in the fourth, and the final redshift z_{end} in the last column. We also carried out the medium-box runs ($l_{box} = 64$ Mpc h^{-1}) with the Enzo code, in both Unigrid and AMR (6 levels) mode for runs up to $N_p = 256^3$ and in Unigrid mode only for $N_p = 512^3$.

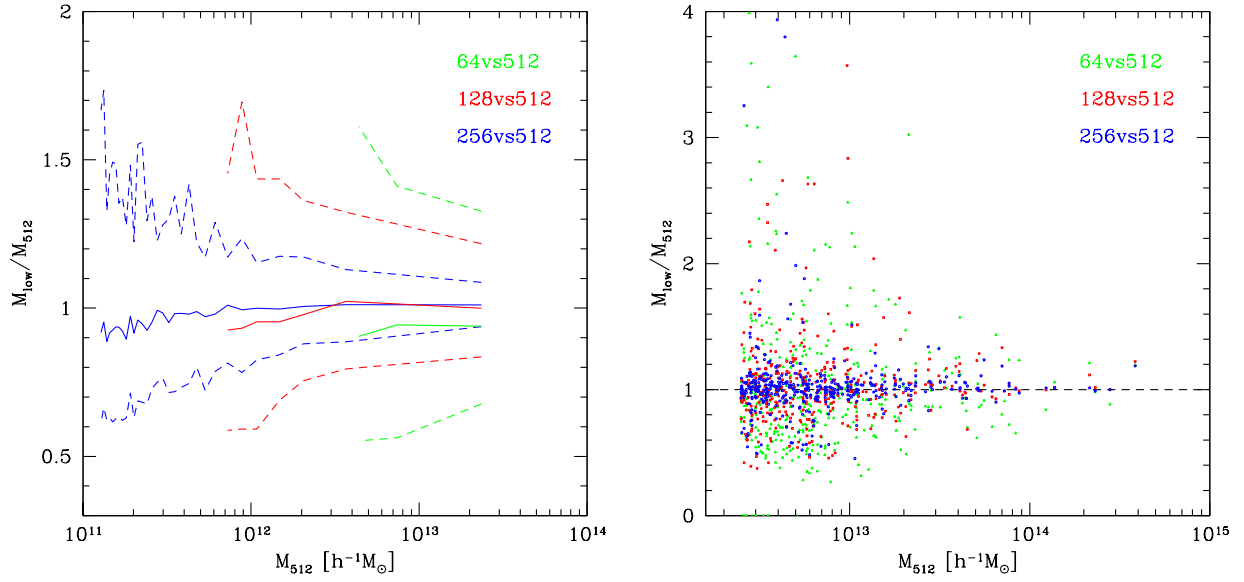


Fig. 1.— Comparison of individual halo masses at $z = 0$ for four realizations of the same initial conditions (medium box: $l_{box} = 64 \text{ Mpc h}^{-1}$) at different resolution, from $N_p = 64^3$ to $N_p = 512^3$. The two panels show the ratio M_{low}/M_{512} of halo mass measured at low resolution against the value found in the highest resolution run as a function of the halo mass at high resolution. Halos have been identified in the high-resolution realization ($N_p = 512^3$) and matched to counterparts at lower resolution. Left panel shows the median of M_{low}/M_{512} as a solid line. Dashed red lines delimit the symmetric 1σ region around median. Color coding is as follows. Green: $N_{low} = 64^3$; red: $N_{low} = 128^3$; blue: $N_{low} = 256^3$. Right panel: zoom into the individual M_{low}/M_{512} values for the most massive halos (identified in all realizations).

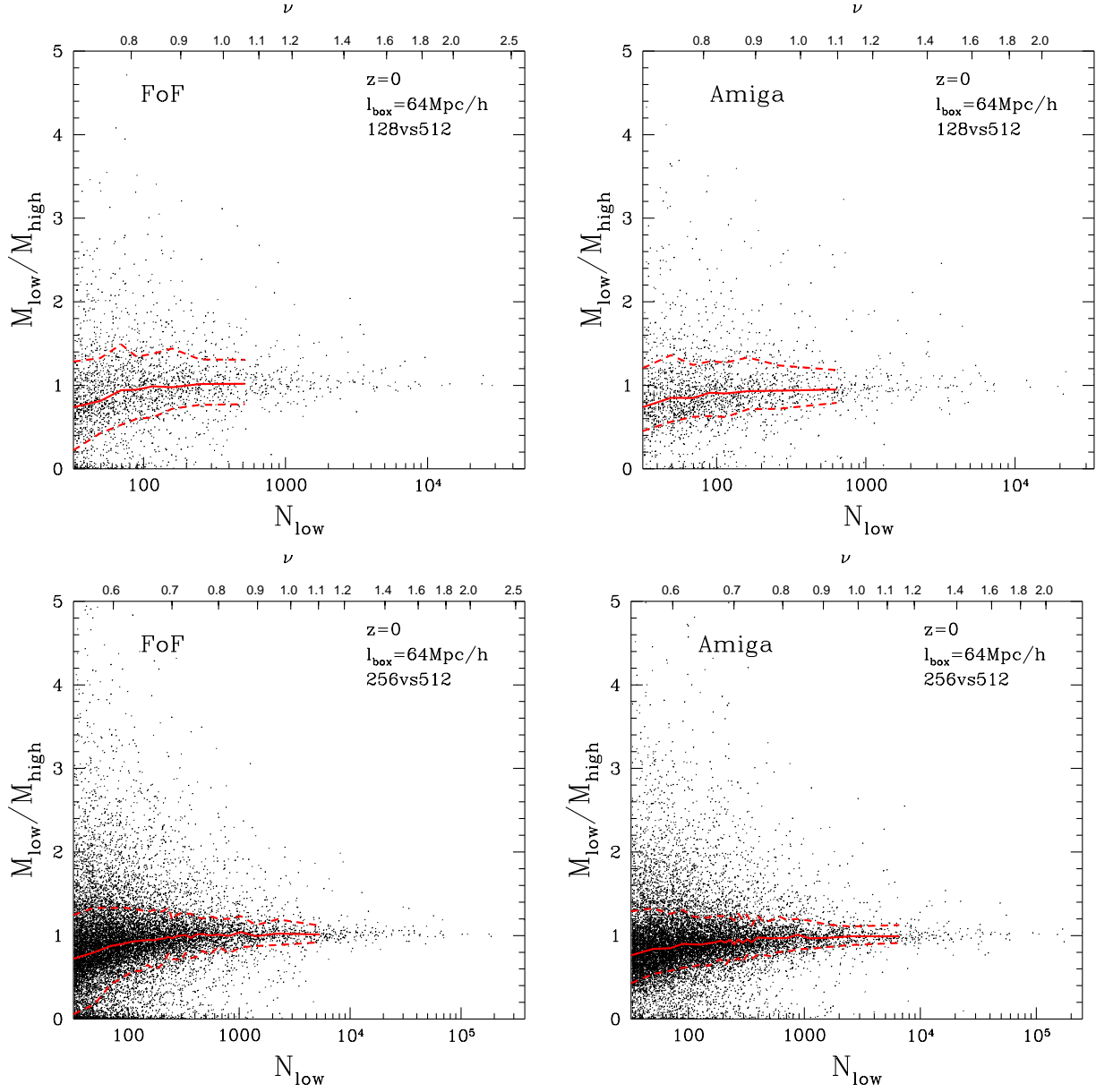


Fig. 2.— Upper left panel: Ratio of low-to-high resolution mass of dark matter halos identified in the $N_p = 128^3$ version of our medium box ($l_{\text{box}} = 64 \text{ Mpc h}^{-1}$) at $z = 0$ and compared to higher resolution realization ($N_p = 512^3$) with same initial conditions. The scatter plot is shown as function of number of low-resolution particles. Solid red line represents median value of ratio, and red dashed lines enclose 1σ symmetric confidence region around median. The upper axis translates halo particle number into dimensionless variable $\nu = \delta_c^2/\sigma^2(M)$, a measure of the rarity of a halo in the extended Press-Schechter formalism. Upper right panel: same as upper left panel, but here dark-matter halos have been identified with Amiga halo finder (Knollmann & Knebe 2009) including removal of unbound particles. Lower left and right panels are same as the upper set, but for $N_p = 256^3$ run compared to $N_p = 512^3$ run.

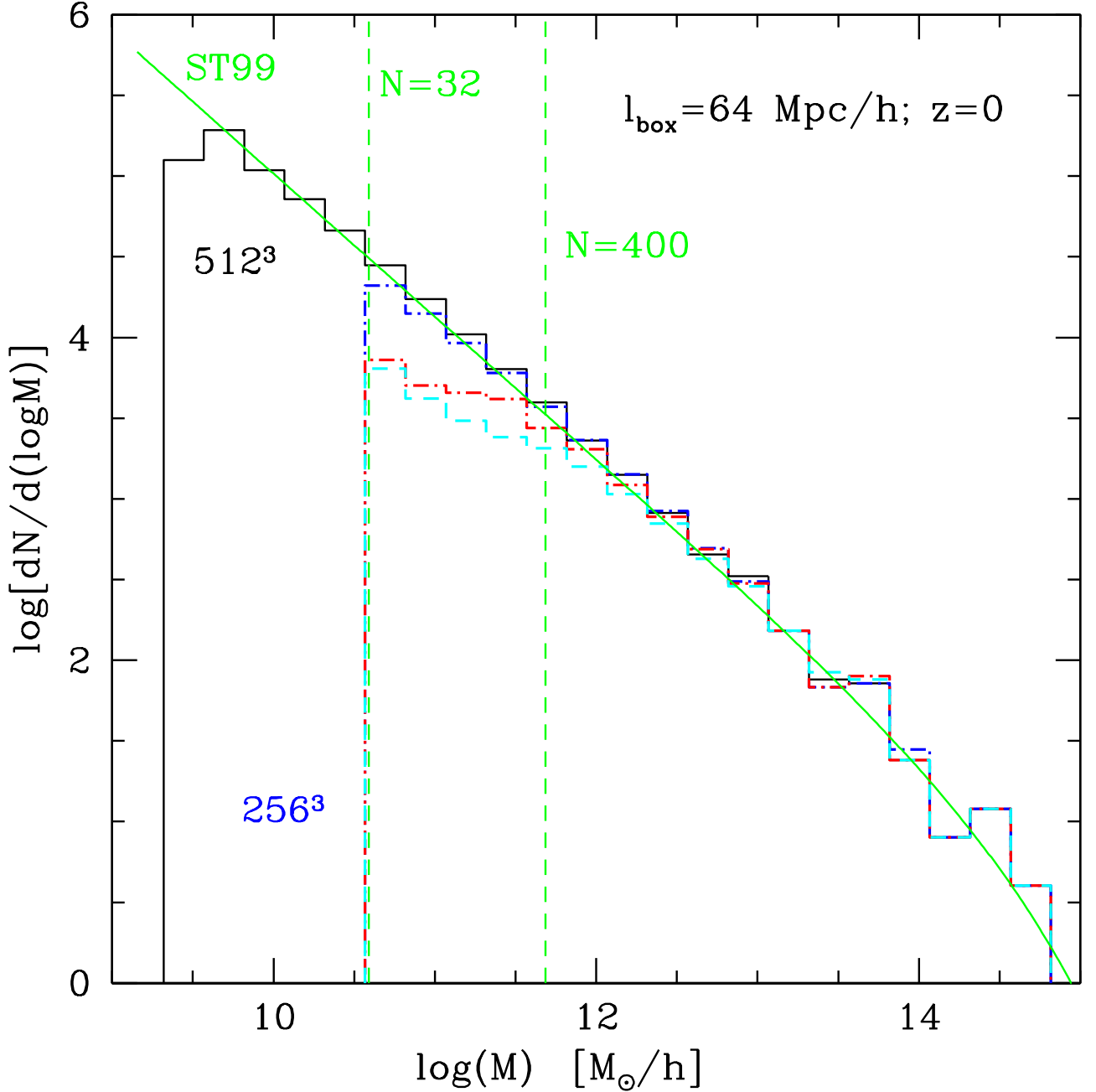


Fig. 3.— Halo mass function at $z = 0$ of medium box simulated with $N_p = 512^3$ particles (black solid line) compared to $N_p = 256^3$ realizations (Gadget2 blue dotted-dashed line; Enzo AMR red dotted-dashed line; Enzo Unigrd cyan dashed line). For comparison, we also plot Sheth & Tormen (1999) halo mass function (solid green line). The low-resolution halo mass function obtained in the Gadget2 run is consistent with high-resolution and analytical mass function down to its resolution limit ($N \sim 30$). The halo mass function from the Enzo runs converges only when $N \gtrsim 400$.

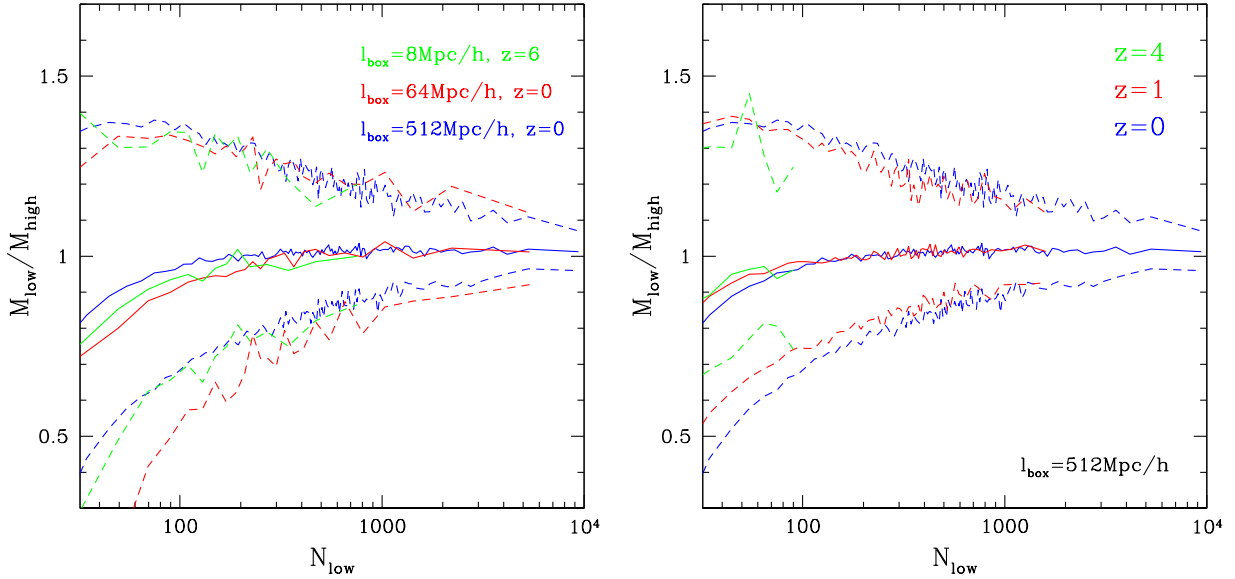


Fig. 4.— 1σ confidence intervals (dashed lines) and median (solid lines) for the ratio of low-to-high resolution mass of dark matter halos as in Figure 2 but considering different simulations. The left panel investigates different box sizes. Blue lines are associated with the $N_{low} = 512^3$ version of our large box ($l_{box} = 512 \text{ Mpc h}^{-1}$) compared to the $N_{high} = 1024^3$ realization at $z = 0$. Red lines refer to $N_{low} = 256^3$ version of medium box ($l_{box} = 64 \text{ Mpc h}^{-1}$) compared to $N_{high} = 512^3$ realization at $z = 0$. Green lines refer to $N_{low} = 256^3$ version of small box ($l_{box} = 64 \text{ Mpc h}^{-1}$) compared to $N_{high} = 512^3$ realization at $z = 6$. Right panel investigates the redshift dependence of convergence for large box realization $N_{low} = 512^3$ compared to $N_{high} = 1024^3$ at $z = 0$ (blue), $z = 1$ (red), and $z = 4$ (green). Halos at fixed number of particles are rarer at higher redshift and have slightly less scatter in the mass measurements.

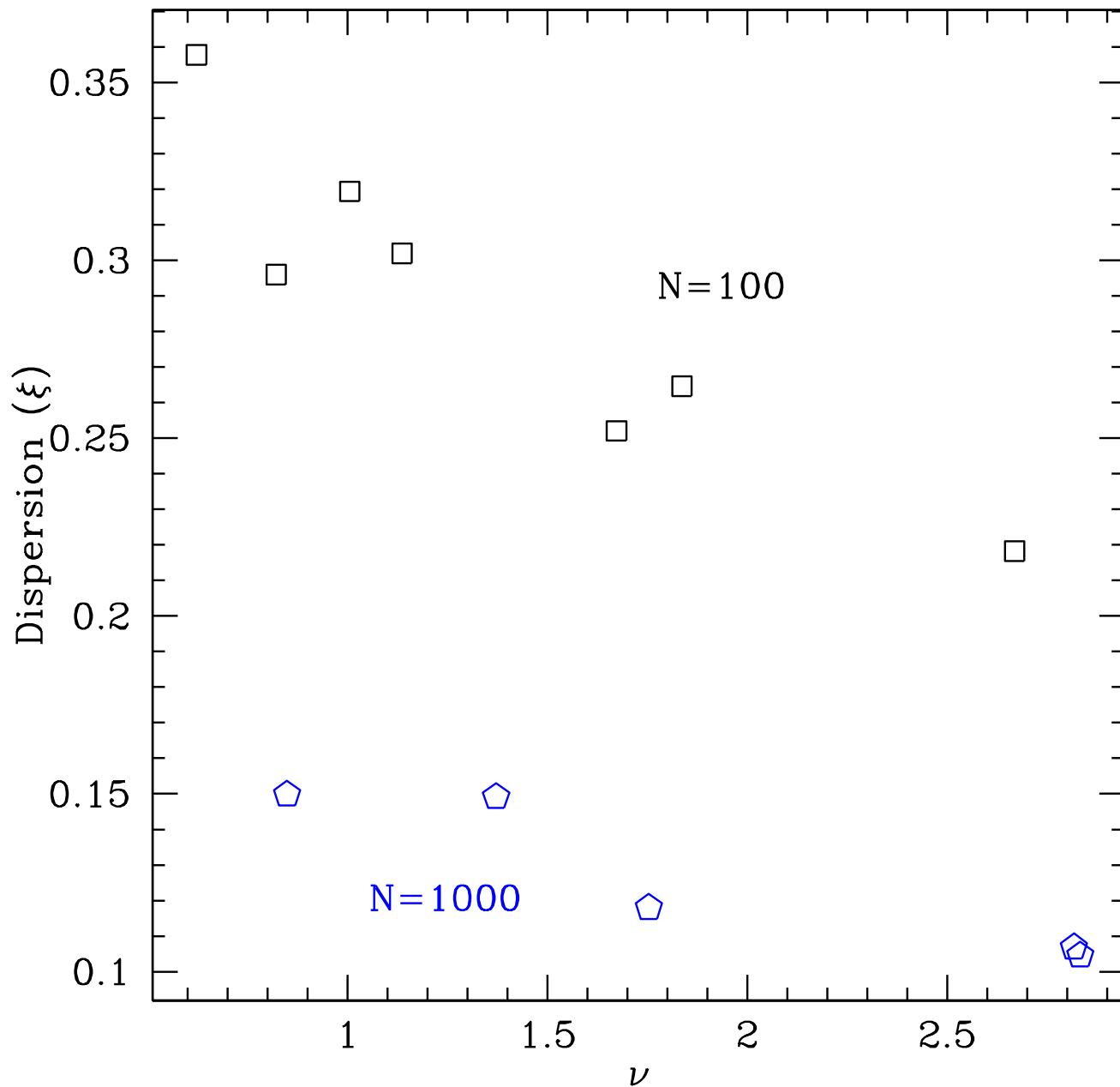


Fig. 5.— The 1σ dispersion ξ around median for M_{low}/M_{high} distribution in our set of simulations considering halos with $100 \leq N_{low} \leq 200$ (black squares) and with $1000 \leq N_{low} \leq 2000$ (blue pentagons) as function of rarity ν . Rare (large ν) halos resolved with a low number of particles have less scatter than their more common counterparts.

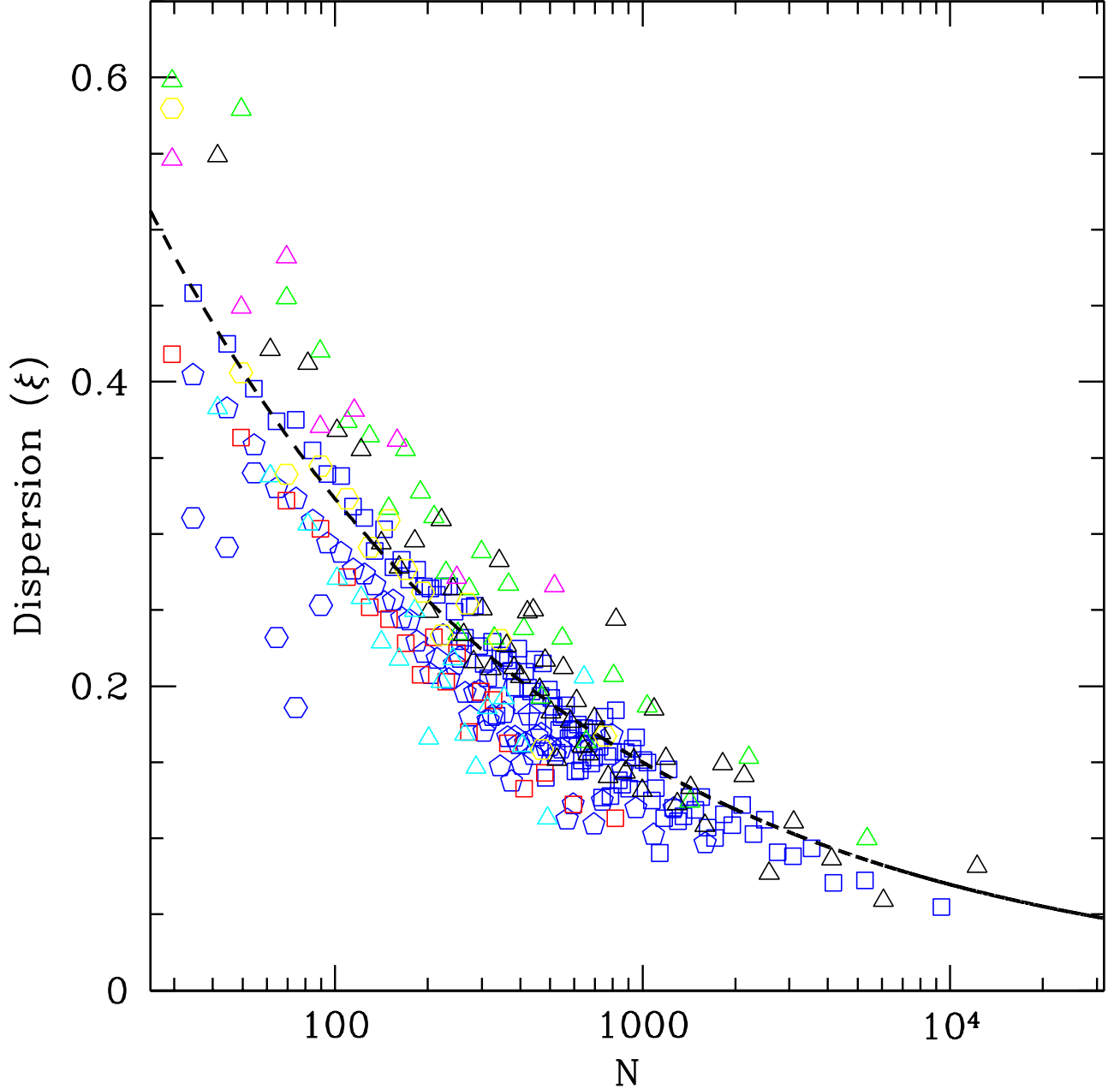


Fig. 6.— The 1σ dispersion ξ around median for M_{low}/M_{high} distribution in our set of simulations as function of number of particles in low-resolution run. Triangles show color-coded results from medium box: common halos in the 256vs512 snapshot at $z = 0$ (green) and at $z = 1$ (black), rarer halos in the $z = 4$ snapshot (light blue) and halos in the 128vs512 snapshot at $z = 0$ (violet). Squares are from large box at $z = 0$ (red 256vs1024; blue 512vs1024). Pentagons are from large box (512vs1024) at $z = 1$ and blue hexagons are from same simulation at $z = 4$, representing halos with smallest $\xi(N)$ (due to their rarity). Yellow hexagons are from small box at $z = 6$ (256vs512). Dashed line represents the analytical scaling predicted in Section 3 ($\xi \propto N^{-1/3}$).

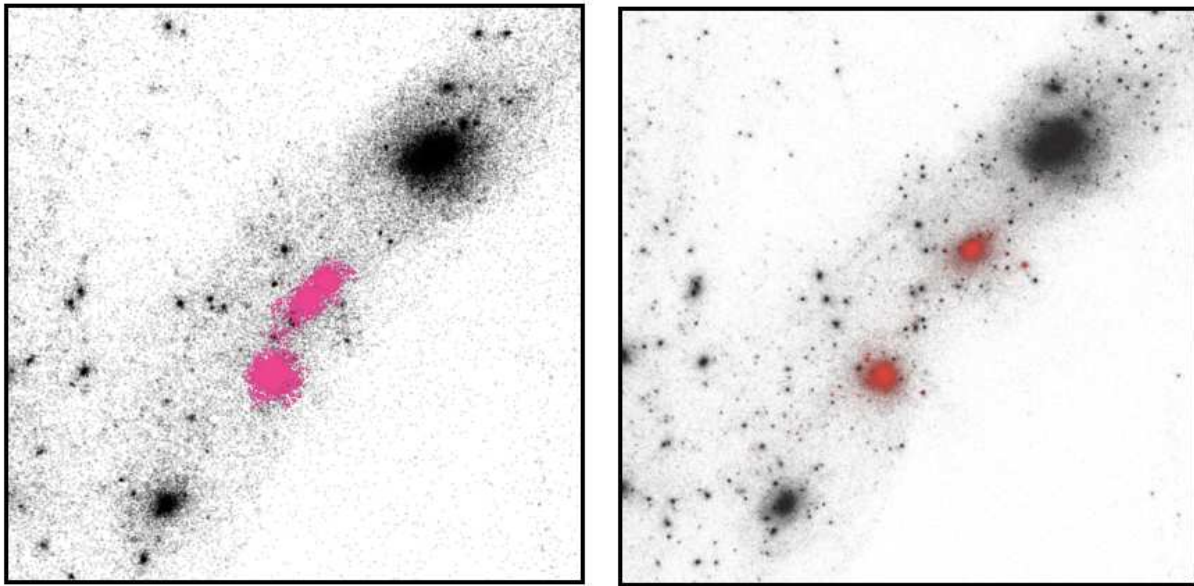


Fig. 7.— $(7 \text{ Mpc } h^{-1})^3$ region around one halo of our medium-box simulations at low resolution (left $N_p = 256^3$) and high resolution (right $N_p = 512^3$). The 8192 particles belonging to the halo at low resolution are shown in magenta (left), while their counterparts at high resolution are in red (right). This halo has two distinct counterparts at high resolution, because the merging is slightly delayed compared to low-resolution realization, where a thin bridge of particles already connects the two sub-components.

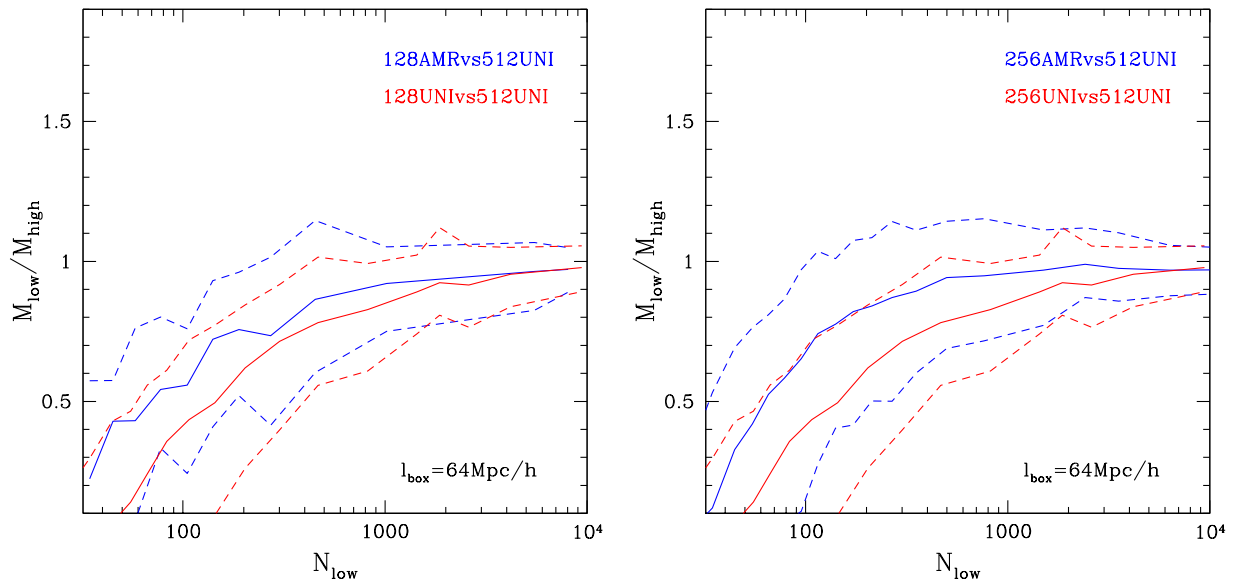


Fig. 8.— Same as Fig. 4 but for runs carried out with the Enzo code. The left panel compares $N_{low} = 128^3$ in Unigrid mode, shown as red lines, and in AMR mode (6 levels), shown as blue lines, to $N_{high} = 512^3$ (Unigrid) at $z = 0$. The right panel is as the left one but for $N_{low} = 256^3$. The mass of individual halos with $N \lesssim 500$ is significantly underestimated in Enzo. AMR helps to improve convergence, but its effectiveness is limited.

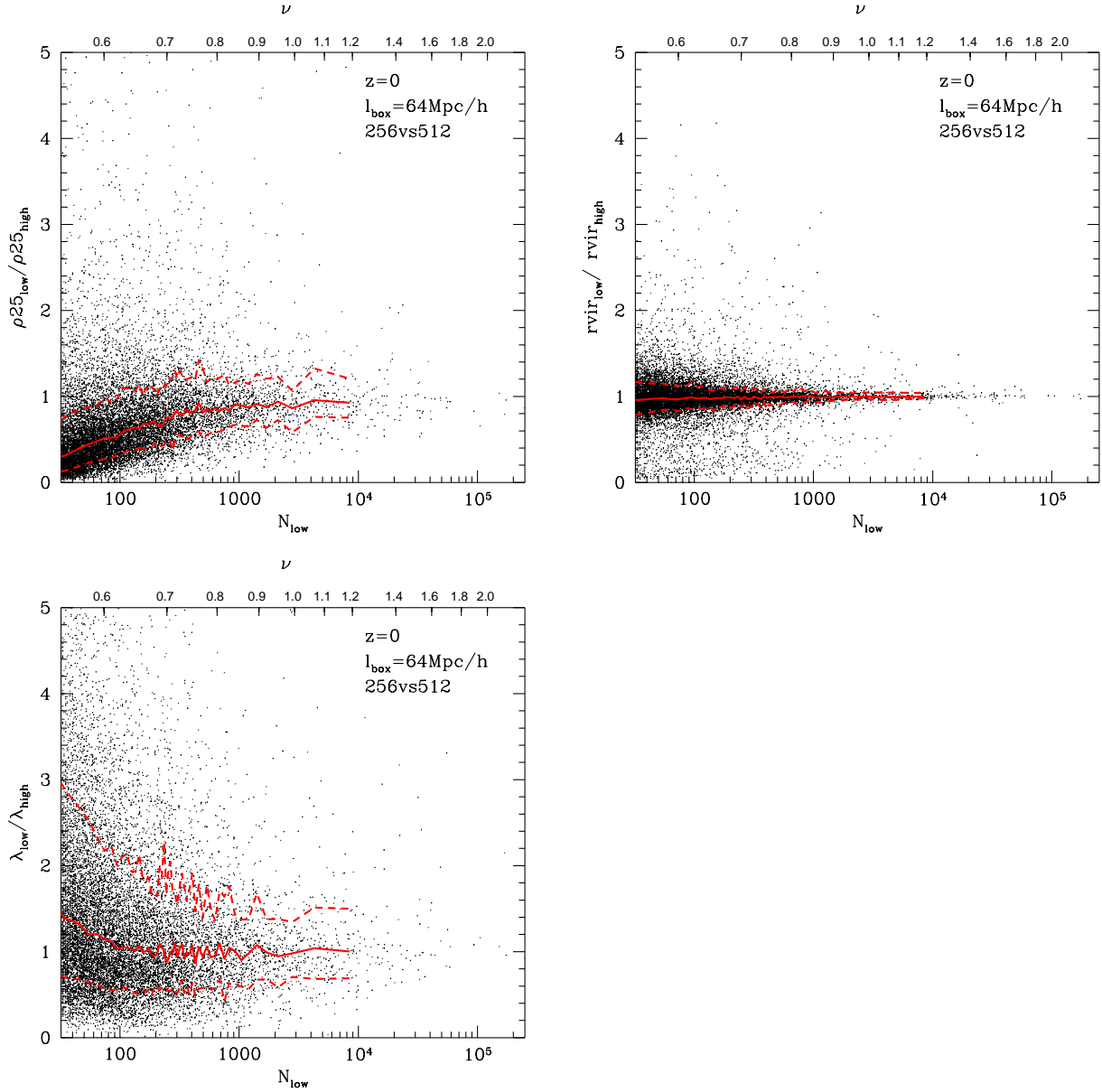


Fig. 9.— Convergence of additional properties of dark matter halos in $N_p = 256^3$ realization of medium box compared to their high-resolution counterparts ($N_p = 512^3$ run). Upper-left panel: Ratio of core density $\rho_{25_{low}}/\rho_{25_{high}}$. Upper-right panel: Ratio of virial radius $r_{vir,low}/r_{vir,high}$. Lower left panel: Ratio of dimensionless angular momentum $\lambda_{low}/\lambda_{high}$. For each panel the solid red line shows the median of distribution. Dashed red lines delimit the symmetric 1σ region around median.